



PII S0016-7037(02)01072-4

## Growth of disk-shaped bubbles in sediments

B. S. GARDINER, B. P. BOUDREAU,\* and B. D. JOHNSON

Department of Oceanography, Dalhousie University, Halifax, Nova Scotia B3H 4J1, Canada

(Received March 5, 2002; accepted in revised form July 22, 2002)

**Abstract**—Disc-shaped methane bubbles, often observed in marine sediments, result from growth in a medium that elastically resists expansion of the bubbles and yields by fracture. We have modeled this process to obtain estimates of growth times by using a reaction-diffusion model coupled to a linear elastic fracture mechanics (LEFM). For comparison, we also modeled the growth of a constant eccentricity bubble in a nonresistant medium. Discoidal bubbles that grow in sediments that obey LEFM grow much faster than spherical bubbles (two- to fourfold faster for the times and conditions tested here) and become more eccentric with time (aspect ratios falling from 0.3 to 0.03 over 8 d of growth). In addition, their growth is not continuous but punctuated by fracture events. Furthermore, under some conditions, LEFM predicts that bubble growth can become arrested, which is not possible for a bubble in a nonresistant medium, even for nonspherical bubbles. Cessation of growth occurs when the dissolved gas concentration gradient near the bubble surface disappears as a result of the increase in bubble gas pressure needed to overcome sediment elasticity. Copyright © 2003 Elsevier Science Ltd

### 1. INTRODUCTION

The production of volatile substances, usually methane, during diagenesis can lead to saturation of the pore waters and the subsequent formation of gas bubbles. The presence of such bubbles can engender significant geochemical and geotechnical consequences, as previously discussed in Martens and Klump (1980) and Hovland and Judd (1992), including greatly enhanced methane fluxes to the atmosphere through ebullition. Given the important effects of bubbles, the dearth in our knowledge of their rates of formation and of the processes that control those rates is surprising. In particular, little solid or systematic estimates of these rates exist, and what we do have is largely in the form of crude deductions of seasonal growth that are based on limited observations in Martens and Klump (1980).

Recently, we undertook a research program to redress this paucity of information by a combined program of bubble growth experiments and theoretical modelling. Our first effort in this field produced a theoretical model of the growth for a spherically shaped bubble in a sediment that does not offer resistance to the expansion of the bubble (Boudreau et al., 2001a,b). This model balances the (methanogenic) production of the volatile solute with its diffusion to the growing bubble to obtain an equation for the radius of the bubble,  $R(t)$ , with time

$$R(t) = \left[ \frac{2\varphi D}{\psi_g} \left\{ \frac{SR_1^2}{6D} + (\psi_1 - \psi_o) \right\} t + R_o^2 \right]^{1/2}, \quad (1)$$

where  $t$  is time,  $\varphi$  is the porosity of the sediment surrounding the bubble (assumed locally constant),  $D$  is the diffusion coefficient for the volatile solute (corrected for tortuosity),  $S$  is the local rate of volatile production (assumed constant on the scale of the bubble),  $\psi_1$  is the solute concentration “far” from the bubble’s influence, i.e., at a distance  $R_1$ ,  $\psi_o$  is the concentration

adjacent to the bubble,  $\psi_g$  is the concentration of gas in the bubble, and  $R_o$  is the initial radius of the bubble (usually assumed to be zero). This equation differs fundamentally from the well-known equation for diffusive growth of a bubble (Scriven, 1959; Barlow and Langlois, 1962) by the presence of the term containing the in situ source  $S$ ; thus, both the degree of supersaturation (second term in the square root) and the surrounding production of the volatile,  $S$ , can drive growth. When realistic values of these parameters for a methanogenic sediment are placed into Eqn. 1, there results growth times for a 1-cm-diameter bubble of  $\sim 20$  to 150 d. Thus, this simple model has provided the first ever predictions of bubble growth times, which appear to suggest subseasonal to seasonal growth times.

Since the appearance of the no-resistance spherical model, we have completed experiments that reveal that sediments do, in fact, oppose bubble growth, often and probably dominantly by elastic yield and fracture (Johnson et al., 2002). These types of interactions with the sediment lead to bubbles that are not spherical, but disk-shaped (discoidal), and often of extreme eccentricity, as verified by X-ray images reported in Abegg et al. (1994), Johnson et al. (2002), and A. Best (personal communication). This discoidal geometry possesses a significantly different surface to volume ratio than that of a sphere, which in turn implies an altered rate of gas accumulation and bubble growth. This fact behooves us to reexamine the predictions made with the simple spherical model found in Boudreau et al. (2001a,b).

Our aim here is to present a new model for discoidal bubble growth in a medium that yields elastically and at critical stress by fracturing, such as we observe in sediments, and to assess the effects of this new geometry and new mechanics on predicted bubble growth rates. Before this model reformulation and solution, we review the pertinent experimental results reported in Johnson et al. (2002), both because they form the basis for parameter selection for our new model and because geochemists may be less familiar with elastic fracture mechanics than, say, fluid dynamics.

\* Author to whom correspondence should be addressed (bernie.boudreau@dal.ca). B. S. Gardner is now at the Department of Mathematics and Statistics, University of Melbourne, Parkville, VIC 3010, Australia

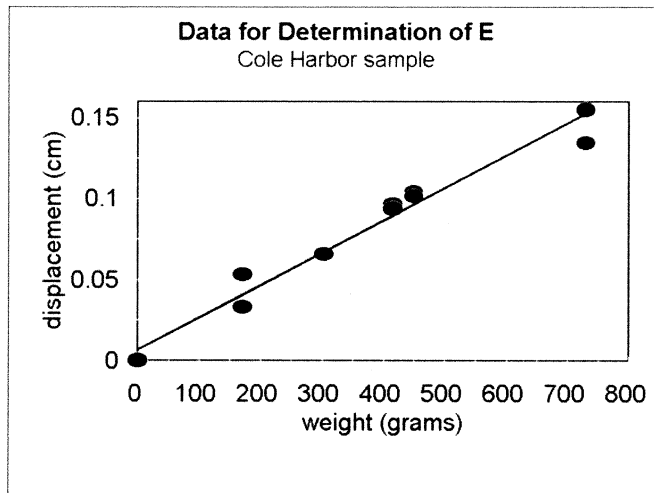


Fig. 1. A plot of the rebound stress-strain data obtained from Cole Harbour sediment (Nova Scotia, Canada). The stress-strain relation in this plot is linear, and the slope is Young's modulus,  $E$ . The linearity of this plot constitutes proof of elastic behavior of these sediments at high stresses. Figure reproduced from Johnson et al. (2002).

## 2. SEDIMENT ELASTICITY AND FRACTURE

If sediments fracture, then they must act mechanically like a solid. This begs the question: what type of solid? All indications point to an elastic solid. The evidence for the elastic behavior of sediments comes from two sources, specifically acoustic propagation and our own direct determinations. Much of the interpretation of acoustic data from sediments is accomplished successfully by assuming that sediments are well described by Hookean (linear) elastic mechanics (e.g., the review by Hamilton, 1980, see particularly the appendix).

One could, of course, argue that acoustics are concerned only with infinitesimal, or at worst, small strains (deformations), whereas bubble growth is a large strain phenomenon. Yet our own experimental evidence presented in Johnson et al. (2002) clearly indicates that marine sediments continue to respond both elastically and linearly to stress until they fail. Specifically, we have measured the elastic *rebound* of muddy sediments from Cole Harbour (Cow Bay), Nova Scotia, and from that data, determined values of Young's modulus, i.e., the relevant Hookean parameter, at strains comparable to those that occur during bubble growth. Figure 1 illustrates the results from such an experiment, where rebound displacement (strain) is plotted against added weight (stress). Clearly this plot is linear, as demanded by Hookean (linear elastic) mechanics.

Next, how do we know that bubbles can grow by fracture of this sediment, as well as elastic deformation? We have collected a considerable amount of experimental data on incremental bubble growth during gas injection into natural sediments. (A detailed description of the experimental setup can be found in Johnson et al., 2002.) Figure 2 illustrates the internal pressure, bubble volume estimated from the pressure-volume product (PV), and added bubble volume (delta V) estimated from small volume perturbations of the system during a bubble growth experiment by gas injection in sediment from Cole Harbour, Nova Scotia, Canada. The large sawtooth pattern of

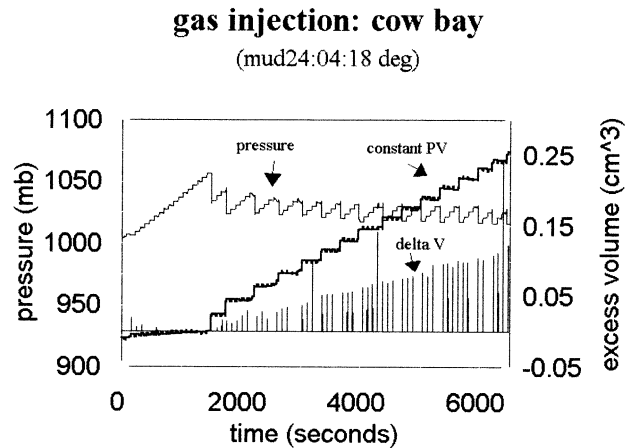


Fig. 2. Plot of the internal pressure, bubble volume estimated from the assumption of constant pressure-volume product (PV), and bubble volume estimated from small perturbations (delta V) of the bubble system during a typical bubble injection experiment as described in Johnson et al. (2002). See Johnson et al. (2002) for a more detailed explanation.

the internal pressure line is the result of elastic growth that is punctuated by fracture of the sediment; that is to say, small injections of gas (the small steps) into the bubble eventually cause the internal pressure to exceed the strength of the sediment. The bubble then grows to a new larger size and reduces the internal pressure to a value given by the bottom of a large step (tooth). Further injections of gas cause the process to repeat. In contrast, if bubble growth occurs in a fluidlike sediment, the pressure line in Fig. 2 would be horizontal as stress cannot be supported, and an illustrative example can be found in Johnson et al. (2002).

In addition, we note that there is no indication in Fig. 2, or any other plots that we have obtained, of subcritical fracture (creep). The evidence in Fig. 2 is of sharp, discrete, and repeatable failure, i.e., the drop in pressure is essentially constant over all fractures. If there were subcritical crack (bubble) growth, the line would be curved by the subcritical effects. Fracture is discrete, occurs essentially instantaneously (not a rate process on our timescales), and indicates essentially the same critical strength of the sediment for each fracture event.

What mechanical model describes fracture in this type of medium? In this regard, Johnson et al. (2002) have demonstrated that the excess pressure inside their bubbles at fracture,  $P_c$ , i.e., that above ambient, is entirely consistent with the linear elastic fracture mechanics (LEFM). Specifically, LEFM demands that  $P_c$  and the bubble volume,  $V_b$ , be related such that, for a (disk) penny-shaped crack

$$P_c \propto V_b^{-1/5}. \quad (2)$$

The data for  $P_c$  and  $V_b$  from one of our bubble experiments in a natural sediment are displayed in Fig. 3. The best-fit straight line possesses a slope of  $-1/5$  with an  $R^2 > 0.9$ , as required by Eqn. 2. Note that if appreciable subcritical behavior were present, then there would be observable deviation from a straight line. Thus, the fracture process is well described by LEFM.

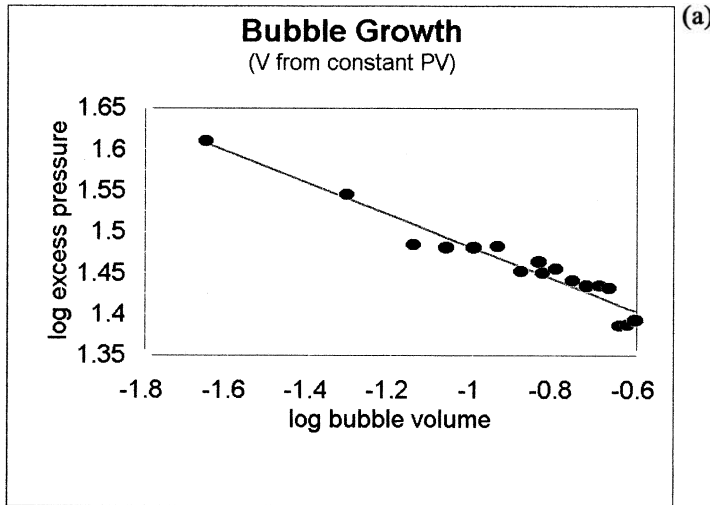


Fig. 3. Plot of the excess pressure in bubbles injected into natural sediments as a function of the corresponding bubble volume. The straight line is a least-squares best fit of Eqn. 2 and has a slope of  $-0.201$  ( $R^2 > 0.9$ ). Taken from Johnson et al. (2002), which also provides details of the experimental setup.

Finally, what is the shape of the bubbles produced by elastic fracture? Figure 4a reproduces an X-ray image of a bubble injected into the Cole Harbour sediments used in the above quoted experiments, as well as some natural bubbles; they are all highly eccentric disk-shaped voids. To verify this result, we have injected gas into gelatin, which has similar mechanical properties to sediments (Johnson et al., 2002). Figure 4b illustrates such a bubble, and it is definitely disk-shaped.

The next step in our development is to link production and diffusion of the volatile in the sediment to a growing discoidal bubble. So as to integrate the diffusion-reaction model with fracture mechanics and thus obtain a growth model.

### 3. DIFFUSION TO A DISCOIDAL BUBBLE

Because the bubbles of interest are disk-shaped, a convenient choice for the geometry of the system is the oblate spheroidal coordinate system (Lebedev, 1972). The mathematical relationships between the normal Cartesian coordinates  $(x,y,z)$  and the oblate spheroidal coordinates  $(\alpha,\beta,\phi)$  are

$$x = c \cosh(\alpha) \sin(\beta) \cos(\phi) \quad (3)$$

$$y = c \cosh(\alpha) \sin(\beta) \sin(\phi) \quad (4)$$

$$z = c \sinh(\alpha) \cos(\beta), \quad (5)$$

where  $c$  is the focal distance,  $\cos()$  and  $\sin()$  are standard trigonometric functions, and  $\cosh()$  and  $\sinh()$  the corresponding hyperbolic functions. Eqns. 3 to 5 indicate that the focal distance,  $c$ , is the crucial scale that links the Cartesian and oblate systems, and it appears in some of the formulas that follow; a geometric explanation of this parameter is provided in Appendix A. The coordinate  $\phi$  plays no role in our subsequent discussions, because of symmetry, and we discuss it no further. This geometric system is illustrated in Fig. 5. Values of the oblate coordinate  $\alpha$  correspond to the ellipses that have their

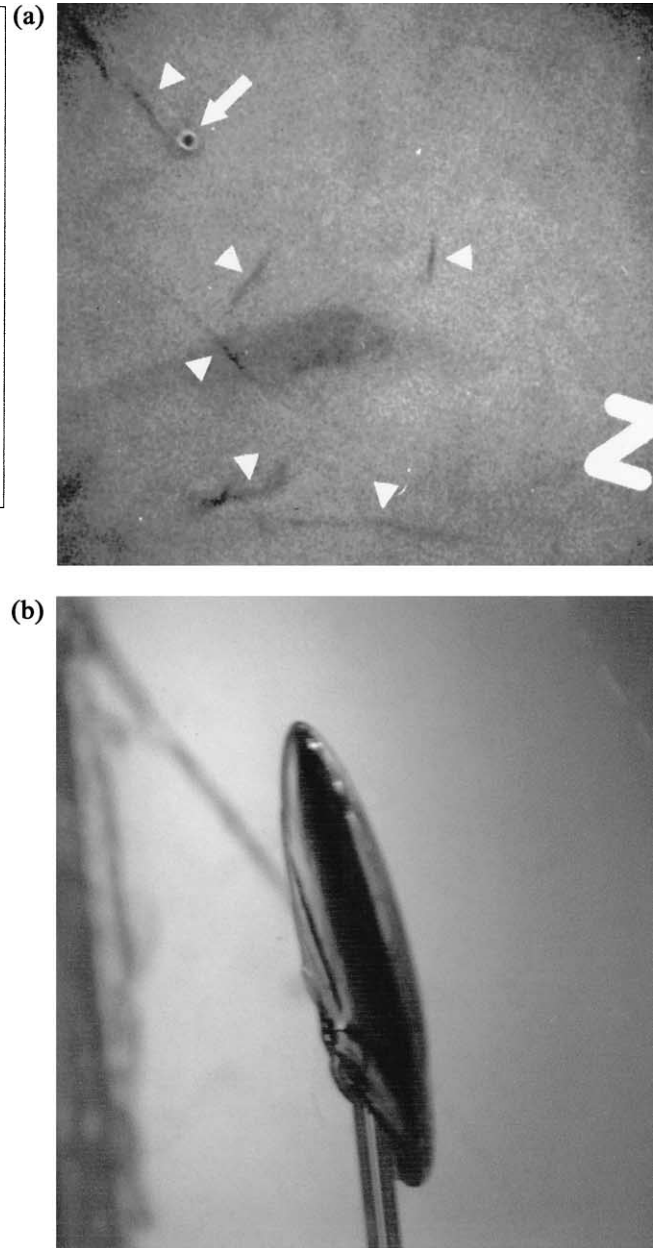


Fig. 4. X-radiograph (Fig. 4a) of a sediment from Cow Bay, Nova Scotia, Canada, with an injected disk-shaped bubble next to an injection tube (indicated by arrowhead near the complete white arrow) and other natural disk-shaped bubbles (indicated by the other arrowheads), as reproduced from Johnson et al. (2002). Figure 4b is a disk-shaped bubble grown in transparent gelatin, which is a good, but transparent, mechanical analog of natural sediment (also reproduced from Johnson et al., 2002.)

major (long) axis along the  $x = 0$  axis and minor axis in the  $z$  direction, whereas the values of the oblate coordinate  $\beta$  are normal to these  $\alpha$  surfaces (Fig. 5a). Specific values of the  $\alpha$  coordinate and corresponding disk cross sections are illustrated in Fig. 5b. Three-dimensional disks are generated by rotating a constant- $\alpha$  ellipse about the  $x = 0$  axis.

It is now possible to state the reaction-diffusion model in the oblate coordinate system. Bubbles grow sufficiently slowly

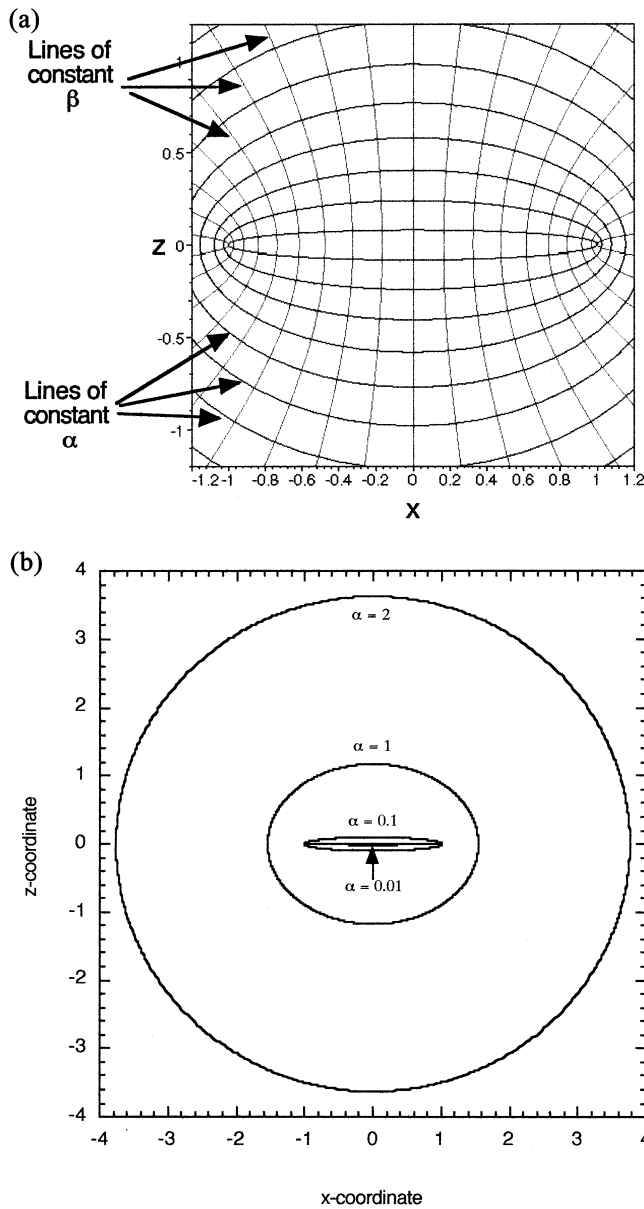


Fig. 5. Illustration in Fig. 5A of the oblate spheroidal coordinate system. Figure 5B contains cross sections for selected  $\alpha$  surfaces. Note that  $\alpha$  surfaces are symmetrical about a rotation in the vertical axis of these diagrams.

(timescale of days or more) that the solute concentration field next to the bubble can readily adjust to maintain a quasi-steady-state configuration, i.e., the diffusion timescale for adjustment is a few minutes at most. Thus, the steady state concentration of a solute,  $\psi$ , in a sediment with a constant distributed gas source  $S$  and diffusion coefficient  $D$ , is given by

$$D\nabla^2\psi + S = 0, \tag{6}$$

where  $\nabla^2$  is the Laplacian operator in oblate spheroidal coordinates, as explicitly given in Lebedev (1972)

$$\nabla^2\psi \equiv \frac{1}{\cosh \alpha} \frac{\partial}{\partial \alpha} \left( \cosh \alpha \frac{\partial \psi}{\partial \alpha} \right) + \frac{1}{\sin \beta} \frac{\partial}{\partial \beta} \left( \sin \beta \frac{\partial \psi}{\partial \beta} \right) + \left( \frac{1}{\sin^2 \beta} - \frac{1}{\cosh^2 \alpha} \right) \frac{\partial^2 \psi}{\partial \phi^2}. \tag{7}$$

The boundary conditions for this problem are similar to those used by previous models for spherical bubble growth (e.g., Boudreau et al., 2001a,b), but modified for the new geometry. At the bubble surface,  $\alpha_0$ , we have equilibrium with the pore-water concentration of methane, i.e.,

$$\psi = k\psi_g \quad \alpha = \alpha_0, \tag{8}$$

In Eqn. 8,  $k$  is Henry's Law constant divided by  $R_gT$  (thus dimensionless), and  $\psi_g$  is the gas concentration within the bubble. Far from the bubble,  $\alpha = \alpha_1$ , the bubble's influence on the concentration field disappears

$$\psi = \psi_\infty \quad \alpha = \alpha_1, \tag{9}$$

where  $\alpha_1$  is a distance far enough away from the bubble for the solute concentration to be essentially unaffected by the presence of the bubble ( $\alpha_0 \ll \alpha_1$ ), and  $\psi_\infty$  is the dissolved gas concentration at  $\alpha_1$ .<sup>1</sup>

Because we are solving a problem for a free (unknown) boundary, i.e., the location of the bubble surface, an additional boundary condition is required. This extra condition takes the form of the statement of mass conservation for the bubble itself

$$\frac{\partial(V_b\psi_g)}{\partial t} = D \int (\nabla\psi \cdot \mathbf{n})_{\alpha=\alpha_0} \partial S, \tag{10}$$

where  $\nabla \cdot$  is the gradient operator in the oblate spheroidal coordinate system,  $\mathbf{n}$  is the outward normal to the bubble surface  $S$ , and  $V_b$  is the bubble volume, which is given by

$$V_b = \frac{4\pi c^3}{3} \sinh(\alpha_0) \cosh^2(\alpha_0) = \frac{4\pi}{3} a^2 b, \tag{11}$$

where  $2a$  and  $2b$  are the major (length or diameter) and minor (width or thickness) axis dimensions of an oblate spheroid, respectively. The left-hand side of Eqn. 10 is the change in the bubble mass (or total moles) with time, whereas the right-hand side constitutes the total diffusive flux across the bubble surface, which is obtained from the solution to Eqn. 10, as in Gardiner et al. (in press). Note that, in this article, bubble aspect ratio is defined as  $E_{cc} = b/a$ ; thus, for a spherical bubble,  $E_{cc} = 1$ .

#### 4. BUBBLE GROWTH IN A FRACTURING ELASTIC MEDIUM

Bubble growth in an elastic medium that is susceptible to fracture occurs in two different ways (phases). If the internal gas pressure is lower than the critical value given by the strength of the material, then the bubble will expand its width,  $b$ , but *not* its length,  $a$ , as it receives gas by diffusion from the surrounding pore waters; that is to say, the sediment will compress elastically as pressure builds in the bubble (the elastic

<sup>1</sup> A bubble-rich sediment could be modeled as a collection of such gas-sediment concentric shells.

Cross-section through an oblate spheroid including the minor axis.

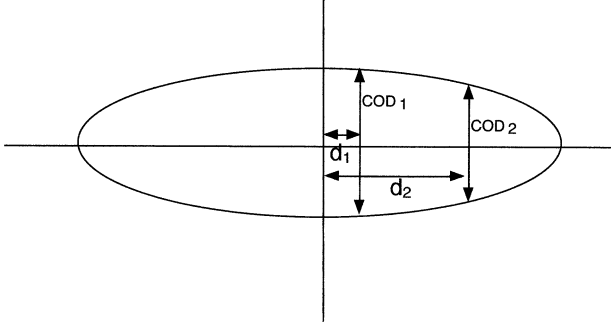


Fig. 6. Illustration of two values of axial distance  $d_1$  and  $d_2$  and the two corresponding crack opening displacements,  $COD_1$  and  $COD_2$ .

phase). When the internal pressure exceeds the strength of the sediment, the sediment fractures and the bubble size and shape readjust according to the governing fracture mechanics and the internal pressure drops to a lower value (Fig. 2). The latter is the fracture phase. The fracture time is sufficiently short (Fig. 2) that diffusion of the volatile solute is negligible during the fracture phase, which in turn means that growth during the elastic and fracture phases can be mathematically decoupled.

#### 4.1. Elastic Phase

We have chosen to model the elastic adjustment of the sediment by using linear elastic mechanics, which is an integral part of LEFM (see Meguid, 1989, i.e., mode I). In this theory, the half-width of the bubble (crack) measured normal from a point on its major axis (Fig. 6) is called the crack opening displacement, COD, and its value is given by the formula

$$COD = \frac{4(P_b - P_0) \sqrt{a^2 - d^2}}{E}, \quad (12)$$

where  $d$  is the distance from the crack center along the crack plane and where  $E$  is Young's modulus. Eqn. 12 can be used to calculate the thickness, and therefore aspect ratio of the disk-shaped bubble, recalling that eccentricity  $E_{cc} = b/a$  and that the maximum bubble thickness,  $b$ , is found by setting  $d = 0$  in Eqn. 12,

$$b = \frac{COD(d=0)}{2} = \frac{2(P_b - P_0)a}{E}. \quad (13)$$

Thus, for a given bubble length  $a$ , if we know the pressure in the bubble,  $P_b$ , we can calculate its shape from Eqn. 12 and its volume from Eqns. 11 and 13. Alternatively, and central to our development, if we know the bubble volume and the internal pressure, or equivalently the gas concentration in the bubble, then the shape of the bubble, i.e.,  $a$  and  $b$ , can be calculated given the validity of the perfect gas law

$$P_b = \Psi_g R_g T. \quad (14)$$

Specifically, if we combine Eqns. 11, 13, and 14, then

$$V_b = \frac{8\pi}{3E} a^3 (\Psi_g R_g T - P_0). \quad (15)$$

Differentiation of this equation with respect to time, by use of the chain rule and Eqn. 15 itself and then expressing the result in terms of  $V_b$ , gives the rate of change of volume of the bubble during the elastic phase as a result of input of gas by diffusion,  $\partial \Psi_g / \partial t$ , i.e.,

$$\frac{\partial V_b}{\partial t} = \frac{3V_b}{a} \frac{\partial a}{\partial t} + \frac{1}{\Psi_g} \left[ V_b + \frac{8\pi P_0 a^3}{3E} \right] \frac{\partial \Psi_g}{\partial t}. \quad (16)$$

During the elastic phase,  $a$  is a constant, and this equation reduces to

$$\frac{\partial V_b}{\partial t} = \frac{1}{\Psi_g} \left[ V_b + \frac{8\pi P_0 a^3}{3E} \right] \frac{\partial \Psi_g}{\partial t}. \quad (17)$$

The change in the internal gas concentration can be calculated from the solution of the diffusion model (see Gardiner et al., in press):

$$\frac{\partial \Psi_g}{\partial t} = \frac{3DX}{2c^2 \cosh(\alpha_0) \left[ \sinh(\alpha_0) + \frac{P_0}{E} \cosh(\alpha_0) \right]}, \quad (18)$$

where the factor  $X$  is given in Appendix B, and  $c$  is the focal distance. The combination of Eqns. 17 and 18 allows calculation of the evolution of the bubble volume during the elastic phase and Eqns. 12 to 14 permits calculation of the shape.

#### 4.2. Fracture Phase

The first question related to this phase is: when will fracture occur? Johnson et al. (2002) have established that the critical bubble gas concentration at which fracture occurs is given by the relation

$$\Psi_{gc} = \frac{\pi^{4/5} (K_{IC})^{6/5}}{24^{1/5} (E V_b)^{1/5} R_g T} + \frac{P_0}{R_g T}, \quad (19)$$

where  $K_{IC}$  is the critical stress intensity factor of the sediment, a quantity that measures the strength of the sediment to fracture. The first values of  $K_{IC}$  to be reported in the literature for sediments can be found in Johnson et al. (2002). The perfect gas law 14 can convert this into an alternative pressure condition.

When fracture occurs, it is assumed to be an instantaneous process (Fig. 2). The sediment cracks a finite length, the bubble now occupies a greater volume, and the pressure falls. We now need to be able to calculate the new bubble shape and volume; unfortunately, there are no guiding principles either within LEFM or within any other related theory that we have examined. (This lack of a suitable theory for postfracture size and pressure adjustments indicates a severe limitation to LEFM that should be rectified.) Thus, to calculate the postfracture size and pressure we must adopt one of two possible assumptions: first, the internal pressure is reduced to a known constant value, or second, the pressure drop may be treated as a known constant. We have decided for the purposes of the present article to adopt the first assumption, which means that there is an internal pressure, above atmospheric pressure, which can be sustained by the sediment allowing the sediment to arrest the fracture. Although this lower pressure is likely to be a function of bubble size, we approximate it as a constant. (We have not used the

constant pressure drop assumption because the critical pressure for fracture decreases with increasing bubble size. Thus, at some point, if we assumed a constant pressure drop, the lower pressure will be below atmospheric.) However, we do not believe that our findings depend crucially on the adopted dynamics.

As stated above, we assume the postfracture internal pressure drops to an ambient value,  $P_a$

$$(P_b)_{pf} = P_a. \quad (20)$$

With this new internal pressure, the new volume of the bubble,  $(V_b)_{pf}$ , can be calculated from the perfect gas law 14, i.e., the number of moles of gas is constant, and thus

$$\frac{(P_b)_{pf}}{P_b} = \frac{(V_b)_{pf}}{V_b}. \quad (21)$$

The new crack (bubble) length is obtained from Eqn. 15 in the form

$$(a)_{pf} = \left[ \frac{3E(V_b)_{pf}}{8\pi((\psi_g)_{pf}R_gT - P_0)} \right]^{1/3} \quad (22)$$

and  $(b)_{pf}$  from Eqn. 13 with the new pressure for  $P_b$ . The new geometry is completely defined and growth in a new elastic phase can begin. During either phase,  $c$  and  $\alpha_0$  can then be determined from  $V_b$  and  $E_{cc}$ , i.e., Eqn. 11 and the relationship

$$E_{cc} = \tanh(\alpha_0). \quad (23)$$

## 5. DIFFUSION LIMITED, CONSTANT ECCENTRICITY BUBBLE GROWTH

To fully understand and appreciate the results of our bubble growth model with fracture, we will compare it to predictions of bubble growth in a medium without resistance. We already have such a model for a spherical bubble, i.e., Eqn. 1. But comparison with the spherical case is not transparent as two effects are confounded, i.e., no resistance and different geometry. To attempt to create a comparison without geometric artifacts, we have solved the problem for growth of a bubble of constant aspect ratio/eccentricity in a medium that offers no resistance. We label this situation the diffusion limited, constant eccentricity (DLCE) case. We emphasize that this scenario is presented for comparative purposes, even if it is not a good representation of true bubble dynamics. In this case,  $\psi_g$  is assumed to be constant throughout bubble growth, as in Scriven (1959), Jones et al. (1999), and Boudreau et al. (2001a,b). This assumption is acceptable if the effects of surface tension are negligible and if the rate of gas transfer to the bubble is small in comparison to bubble size relaxation rate (hence diffusion limited).

In the DLCE model, the change in volume of the bubble is given by

$$\frac{\partial V_b}{\partial t} = \frac{4\pi cDX \cosh(\alpha_0)}{\psi_g}, \quad (24)$$

where the factor  $X$  is the same complex parameter grouping as in Eqn. 18 and that is defined in the Appendix B. In terms of the change in the focal distance  $c$  of the oblate spheroid (see Lebedev, 1972), the equivalent equation is

$$\frac{\partial c}{\partial t} = \frac{DX}{c\psi_g \sinh(\alpha_0)\cosh(\alpha_0)}. \quad (25)$$

Note that when  $\alpha_0 \gg 1$ , i.e., when the bubble is nearly spherical, the spherical bubble solution, Eqn. 1, can be analytically obtained by integrating Eqn. 25.

In the DLCE calculations that follow, the volume, defined by  $c$  and  $\alpha_1$ , is held constant by adjusting  $\alpha_1$  as  $c$  increases; furthermore,  $\alpha_1$  is sufficiently large that the volume defined approximates a sphere, and  $R_1 = c \cosh(\alpha_1)$  is a constant. In particular, we set  $R_1 = 0.03$  m (see Boudreau et al., 2001a,b). For reference, we have applied the DLCE model to the conditions encountered at Cape Lookout Bight; see Boudreau et al. (2001a) for details of the parameter values. The results are presented in Fig. 7. It is apparent from Fig. 7 that highly eccentric bubbles grow to a substantial size in well under a monthly time-scale, when the methane source strength  $S$  is set to the average summer value observed at 10 to 18 cm depth at the Cape Lookout Bight site (Martens and Klump, 1980), which was our previous benchmark (Boudreau et al., 2001a,b). As expected from the relative increase in surface area, a smaller value of  $E_{cc}$  significantly increases the rate of bubble growth. In addition, if we express the size of the DLCE oblate bubble in terms of the radius of a spherical bubble of equivalent volume,  $R_{eq}$ , then the general evolution of the DLCE nonspherical bubbles is such that  $R_{eq} \propto t^{1/2}$ , which is also the behavior noted for spherical bubbles (Scriven, 1959; Boudreau et al., 2001a,b) and in other systems (Glazier and Weaire, 1992).

## 6. MODEL RESULTS AND DISCUSSION

The predictions of bubble growth in an elastic medium that can fracture are displayed in Fig. 8 for the Cape Lookout Bight parameter values. Figure 8 plots the time predicted by LEFM, as well as the DLCE model for  $E_{cc} = 1$  and 0.036, to generate a bubble of a volume equivalent to a 5-mm-diameter spherical bubble. The critical stress intensity factor,  $K_{IC}$ , and Young's Modulus,  $E$ , were not available for the Cape Lookout Bight site. Instead, as an approximation, we employed the values obtained by Johnson et al. (2002) for marine sediments at a site in Cole Harbour (Cow Bay), Nova Scotia, Canada. The values are  $E = 1.4 \times 10^5$  Nm<sup>2</sup> and  $K_{IC} = 300$  N/m<sup>3/2</sup>. It is not expected that the corresponding values of these parameters at Cape Lookout Bight would differ by more than an order of magnitude.

Figure 8a includes DLCE model results for a bubble with  $E_{cc} = 0.036$ , as well as the spherical case where  $E_{cc} = 1$ . The volume of the DLCE model bubble with  $E_{cc} = 0.036$  grows to an equivalent spherical radius of 5 mm in the same time as the LEFM bubble, i.e.,  $\sim 8$  d. However, initially, the LEFM bubble grows more slowly than DLCE model bubble. The growth rate of the LEFM bubble is initially reduced as a result of the bubble size-dependent fracture criteria, which forces the bubble's internal pressure to build-up before growth (Fig. 8b) and the aspect ratio to be more spherical (Fig. 8c). In the long term, however, the fracturing bubble grows faster than the corresponding DLCE bubble, as the average LEFM bubble's aspect ratio falls below 0.036, which is consistent with the small aspect ratios of the bubbles in Fig. 4a.

Because of the fracturing process, LEFM bubbles do not

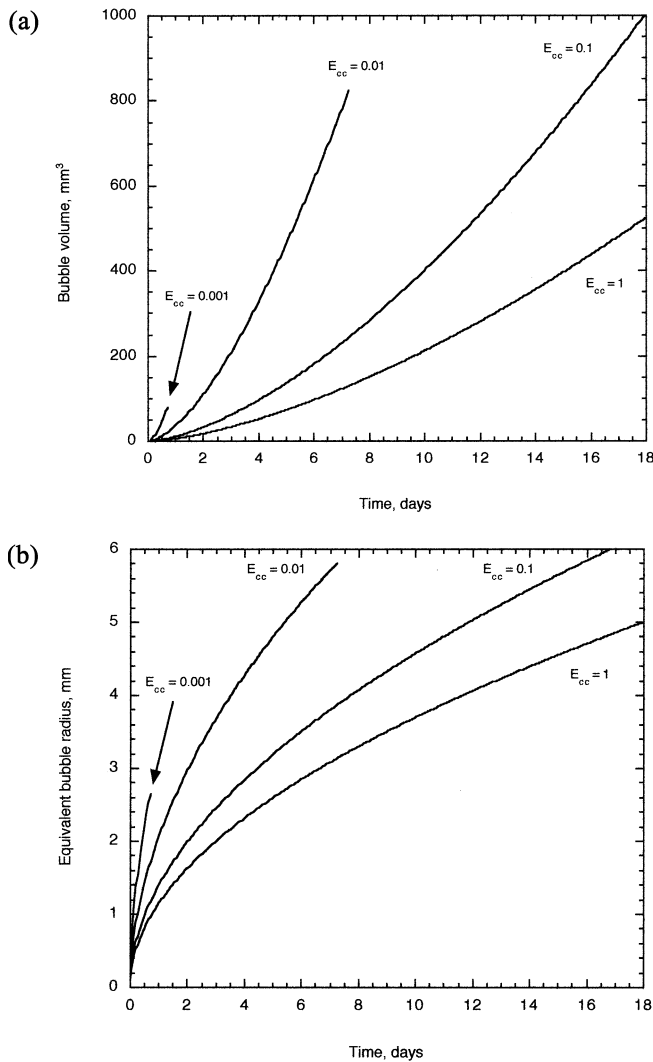


Fig. 7. Bubble volume (Fig. 7A) and equivalent bubble radius  $R_{eq}$  (Fig. 7B) for constant aspect ratio oblate bubbles. Note that the equivalent radius is obtained from a spherical volume having the same volume as the oblate spheroid. The model parameters are those for the Cape Lookout Bight site (Boudreau et al., 2001a)—that is,  $S = 3.47 \times 10^{-6}$  mM/s,  $D = 10^{-9}$  m<sup>2</sup>/s, Henry's constant =  $5 \times 10^7$  Pa/M,  $T = 282$  K,  $R_1 = 0.03$  m, and  $\psi_g = 0.07$  mol/L. Because it is assumed that methanogenesis is the limiting process,  $\psi_\infty$  is set equal to  $k\psi_g$ . Calculations are terminated when bubble dimensions approach  $R_1$ , as seen for  $E_{cc} = 0.001$  and  $0.01$ .

grow smoothly. As seen in Fig. 8a, small-scale variations appear in the growth curve near the beginning of fracturing while the bubble is still small and the critical pressure is large in comparison with surrounding pressure. These small-scale volume variations correspond to large jumps in both the bubble pressure and aspect ratio (Figs. 8b, c).

The right-hand axis of Fig. 9 supplies the ratio of the times needed to grow an oblate bubble of an equivalent spherical radius of 5 mm to that of a true spherical bubble of that same volume. From these results, it is evident that oblate bubbles with smaller aspect ratios have dramatically greater bubble growth rates. Bubble growth with fracture forces the aspect ratio to be much less than unity, i.e.,  $E_{cc} \ll 1$ ; therefore, bubbles

are capable of growing considerably faster in elastic-fracturing sediments than previous spherical models would suggest, i.e., by a factor of two to four over the predictions in Boudreau et al. (2001a,b). The increased growth rate can be attributed to the greater surface-area-to-volume ratio of discoidal bubbles.

To summarize the results, Fig. 8a would at first suggest that LEFM bubble growth is dominated by the elastic response, because the fractures appear to produce minor punctuations in the growth curve; however, the (nine) fractures (Fig. 8c) cause the growth to accelerate away from the spherical growth curve and to surpass the  $E_{cc} = 0.036$  curve in 8 d (Fig. 9), all the result of the increasing eccentricity that results from the fractures (Fig. 8c). Thus, both the growth rate and the shape of an LEFM bubble are dominated by the fracturing, not the elastic growth.

When bubble growth is plotted as a function of the methane source strength  $S$  (Fig. 10), then the fixed aspect ratio DLCE model predicts that the growth time is always proportional to  $S^{1/2}$ , for  $S > 0$  (Gardiner et al., in press); that is, the DLCE model predicts bubbles will grow for all positive values of  $S^{1/2}$  (with  $\psi_\infty - k\psi_g \geq 0$ ). This latter result contrasts with the unexpected predictions from LEFM. LEFM growth times are also proportional to  $S^{1/2}$ , but only for  $S$  above a critical positive, nonzero value (Fig. 10). Below this critical source strength bubbles do not grow!

The no-growth condition arises as a result of the mechanical resistance of the sediment surrounding the bubble. Unlike the DLCE model, LEFM allows the gas concentration in the bubble  $\psi_g$  to vary during bubble growth. For a bubble to grow in an elastic medium, such as sediment, the bubble's internal pressure, and hence gas concentration, needs to rise. Under some conditions (e.g., low  $S$ ; Fig. 10a) or low  $\psi_\infty - k\psi_g$  (Fig. 11), the equilibrium concentration in the bubble ( $k\psi_g$  at  $\alpha_0$ ) can rise quickly enough to produce a zero gradient in dissolved gas concentration at the bubble's surface. In this case, there is no net flux of dissolved gas to the bubble, thereby halting further bubble growth. The volatile (methane) then simply diffuses out across the external boundary  $\alpha = \alpha_1$ . With the wide range in possible sediment conditions, the presence of "stable" non-growing bubbles could be expected, but we have no data with respect to this phenomenon.

Not only is this no-growth regime not found in the DLCE bubble growth models, it is also not to be found in diffusion models for bubbles in Newtonian and power-law viscosity fluids. Newtonian and power-law fluids are unable to support a stress, and so any increase in internal bubble pressure above ambient pressure will eventually result in bubble growth. This is not the case in an elastic medium, such as (most?) sediments.

Bubble growth has so far been assumed to be driven by the source strength  $S$ . Bubble growth can also be driven by the ambient concentration difference,  $\psi_\infty - \psi_g$ , such as in the sediments of Eckernförde Bay in Germany, as shown by Boudreau et al. (2001a). Eckernförde Bay sediments are gassy and have been characterized in reports by Richardson (1994), Wever (1994, 1995), and Martens and Albert (1995). In contrast to the Cape Lookout Bight site, the Eckernförde Bay site may be approximated as a case where  $S = 0$ , as surrounding methanogenesis is not the dominant source of methane for bubble growth. Instead, the ambient methane store is the main contributor to bubble growth Boudreau et al. (2001a). Both the

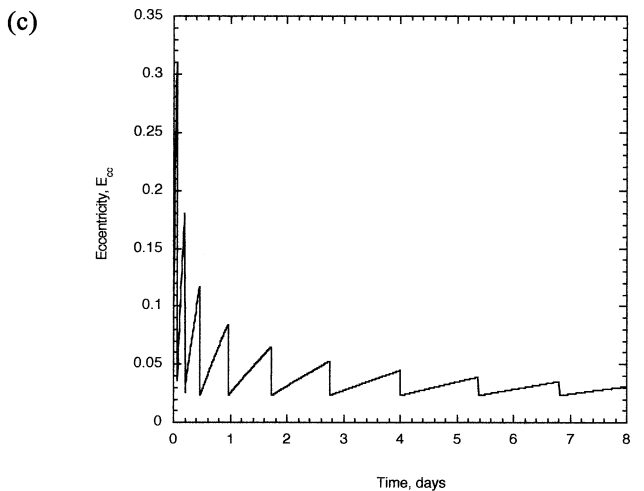
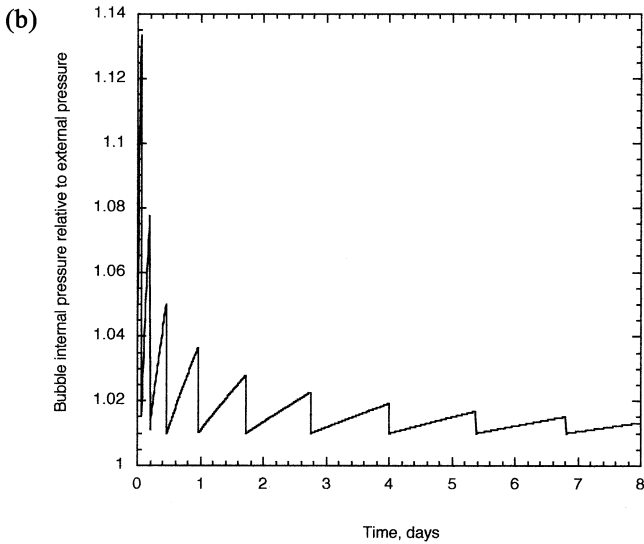
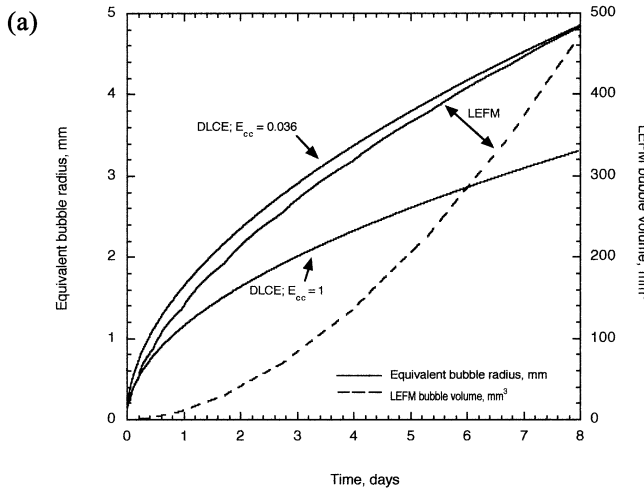


Fig. 8. Bubble growth in a fracturing sediment. Bubble volume and equivalent bubble radius (Fig. 8a), bubble internal pressure (Fig. 8b), and aspect ratio (Fig. 8c) as a function of time for conditions typical of a marine sediment. Included in Fig. 8a are results of a DLCE model with  $E_{cc} = 0.036$ . Parameter values are the same as for Fig. 7 with the addition of  $E = 1.4 \times 10^5 \text{ Nm}^2$  and  $K_{IC} = 300 \text{ N/m}^{3/2}$ .

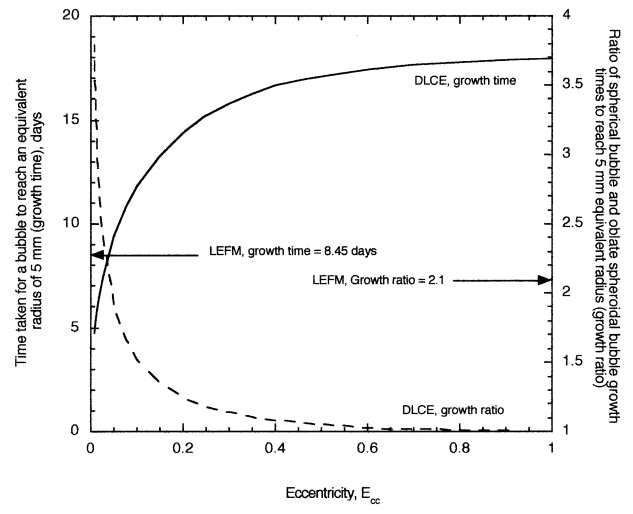


Fig. 9. Comparison of the time it takes a bubble to reach an equivalent radius of 5 mm and the growth rate relative to the spherical bubble DLCE model for DLCE and LEFM model eccentric bubbles, under the conditions used in Figs. 8 and 9.

DLCE model and LEFM were applied to this case. As can be seen in Fig. 12, both the DLCE model and LEFM predict that bubbles will undergo substantial growth within 1 to 3 weeks and that several bubbles may be produced at this site each season.

Finally we would like to remark on an aspect of LEFM that has not been displayed in results previous to Fig. 11. The critical gas concentration at which fracture is initiated is inversely dependent on bubble size, see Eqn. 17. Under some conditions, such as those encountered at Eckernförde,  $\psi_{gc}$  is reduced by bubble growth to a point at which  $\psi_{gc} = \psi_{g0}$ ; that is, the lower critical bubble gas concentration. At this point,

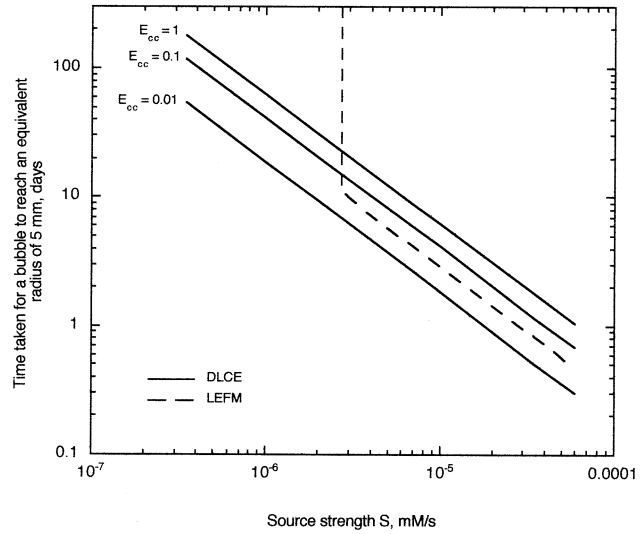


Fig. 10. The effect of source strength on bubble growth times for LEFM and for various bubble eccentricities in the DLCE model. Note that LEFM predicts that at low source strength bubbles will cease to grow. Model parameters are the same as used in Figs. 7 and 8.

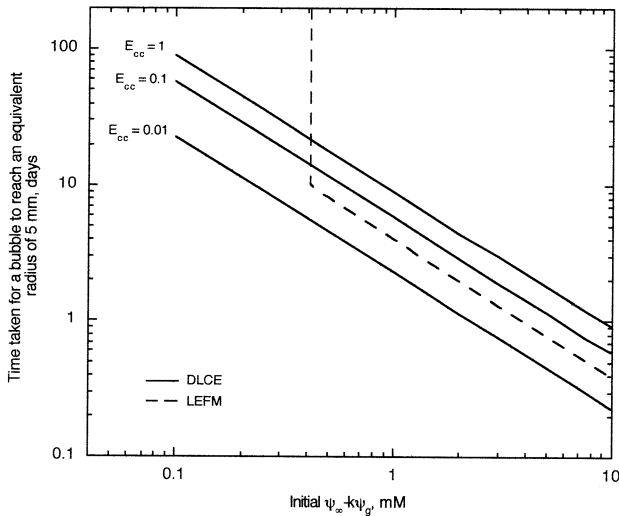


Fig. 11. The effect of initial boundary dissolved gas concentrations on bubble growth times for LEFM and for various bubble eccentricities. Model parameters are the same as used in previous graphs except that now  $S = 0$  and, in general,  $k\psi_g - \psi_{\infty} < 0$ . LEFM predicts that bubbles will cease to grow under certain low dissolved gas replenishment rates, marked by the vertical dashed line.

LEFM theory does not apply because there is no resistance to growth by fracture, and perhaps another model such as DLCE would then be appropriate.

## 7. CONCLUSIONS

We have produced a model for the growth of discoidal methane bubbles in elastic sediments that yield by fracture, and

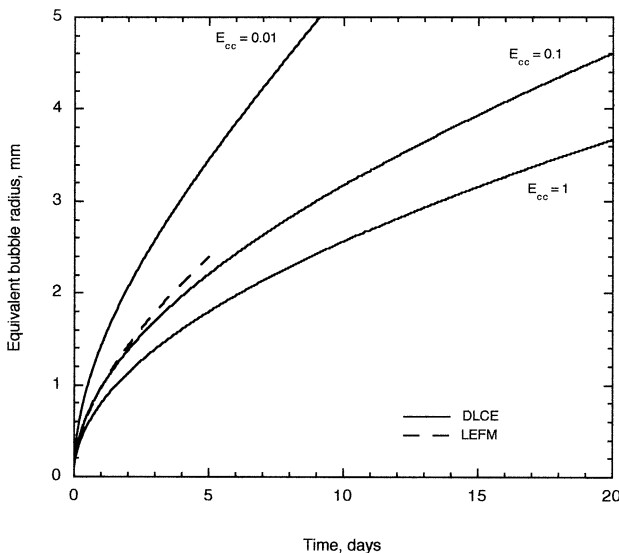


Fig. 12. Combination of DLCE and LEFM results for conditions consistent with observation at the Eckernförde Bay site (Boudreau et al., 2001a). That is,  $S = 10^{-8}$  mM/s,  $D = 5 \times 10^{-10}$  m<sup>2</sup>/s, Henry's constant =  $5 \times 10^7$  Pa/M,  $T = 282$  K,  $R_1 = 0.03$  m, initial  $\psi_g = 0.14$  mol/L, initially  $\psi_{\infty} - k\psi_g = 1$  mM,  $E = 1.4 \times 10^5$  Nm<sup>2</sup>, and  $K_{1C} = 300$  N/m<sup>3/2</sup>. In this case, the ambient store of methane from the boundary defined by  $\alpha_1$  is the dominant methane source; therefore, Eckernförde Bay is effectively a case with  $S = 0$ .

we have compared the results of this model to the situation where the sediment offers no resistance, i.e., pure diffusion control. The disk-shaped bubbles are predicted to form on a weekly timescale, which is faster than possible for spherical bubbles. The evolution of a discoidal bubble is also far more complex than that of a bubble, spherical or discoidal, in a nonresistant medium, with periods of elastic growth punctuated by episodes of fracture growth. The shape of bubbles in an elastic-fracturing medium is also dynamic, becoming more eccentric with time. Overall, both the growth rate and shape of a bubble in an elastic-fracturing sediment are dominated by the effects of the fracturing events. Furthermore, bubble growth in the fracturing case may become arrested by the mechanical resistance of the medium under "weak" methane source strength conditions.

Associate editor: E. Merino

## REFERENCES

- Abegg F., Anderson A., Buzi L., Lyons A. P., and Orsi T. H. (1994) Free methane concentration and bubble characteristics in Eckernförde Bay, Germany. In *Proceedings of the Gassy Mud Workshop, Kiel, 11–12 July, 1994* (ed. T. F. Wever), pp. 84–89. Forschungs Bundeswehr Wassershall Geophysik.
- Barlow E. J. and Langlois W. E. (1962) Diffusion of gas from a liquid into an expanding bubble. *IBM J.* **6**, 329–337.
- Boudreau B. P., Gardiner B. S., and Johnson B. D. (2001a) Rate of growth of isolated bubbles in sediments with a distributed diagenetic source of methane. *Limnol. Oceanogr.* **46**, 616–622.
- Boudreau B. P., Gardiner B. S., and Johnson B. D. (2001b) Erratum to "Rate of growth of isolated bubbles in sediments with a distributed diagenetic source of methane." *Limnol. Oceanogr.* **46**, 1578.
- Broek D. (1982) *Elementary Engineering Fracture Mechanics*. Martinus Nijhoff.
- Gardiner B.S., Boudreau B.P., and Johnson B.D. (in press) Growth of a disk-shaped bubble in the presence of a distributed source of gas. *Appl Math Modelling* (in press).
- Glazier J. A. and Weaire D. (1992) The kinetics of cellular patterns. *J. Phys. Condens. Matter* **4**, 1867–1894.
- Hamilton E. L. (1980) Geoacoustical modeling of the sea floor. *J. Acoust. Soc. Am.* **68**, 1313–1340.
- Hovland M. and Judd A. G. (1992) The global production of methane from shallow submarine sources. *Cont. Shelf Res.* **12**, 1231–1238.
- Johnson B. D., Boudreau B. P., Gardiner B. S., and Maass R. (2002) Mechanical response of sediments to bubble growth. *Mar. Geol.* **187**, 347–363.
- Jones S. F., Evans G. M., and Galvin K. P. (1999) Bubble nucleation from gas cavities—A review. *Adv. Colloid Interface Sci.* **90**, 27–50.
- Lebedev N. N. (1972) *Special Functions and their Applications*. (ed. and transl. R. A. Silverman) Dover Publications.
- Martens C. S. and Klump J. V. (1980) Biogeochemical cycling in an organic rich coastal marine basin—I. Methane sediment–water exchange processes. *Geochim. Cosmochim. Acta* **44**, 471–490.
- Martens C. S. and Albert D. B. (1995) Biogeochemical processes controlling concentrations and transport of biogenic methane in organic rich coastal sediments. In *Proceedings of the Workshop on Modelling Methane-Rich Sediments of Eckernförde Bay, Eckernförde, 26–30 June, 1995* (ed. T. F. Wever), pp. 10–17. Forschungs Bundeswehr Wassershall Geophysik.
- Meguid S. A. (1989) *Engineering Fracture Mechanics*. Elsevier Science Publishers.
- Richardson M. D. (1994) Investigating the coastal benthic boundary layer. *EOS* **75**, 205–206.
- Scriven L. E. (1959) On the dynamics of phase growth. *Chem. Eng. Sci.* **10**, 1–13.
- Wever T. F. ed. (1994) *Proceedings of the Gassy Mud Workshop, Kiel, 11–12 July, 1994*, Forschungs. Bundeswehr Wassershall Geophysik.

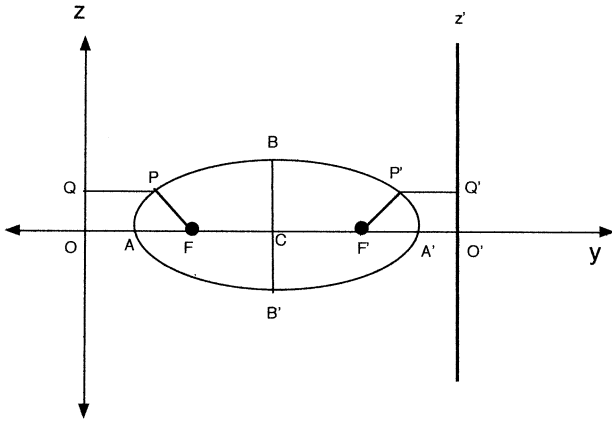


Fig. A1. Plot of a plane cutting through an oblate spheroid that includes the minor axis. The result is an ellipse. The focal points are the points F and F'. The focal distance is distance between F and F'.

Wever T. F. ed. (1995) *Proceedings of the Workshop on Modelling Methane-Rich Sediments of Eckernförde Bay, Eckernförde, 26-30 June, 1995* Forschungs. Bundeswehr Wasserschall Geophysik.

**APPENDIX A**

To provide a geometric explanation for the focal distance  $c$ , consider a plane that cuts an oblate spheroid through its minor axis; the result is an ellipse, as in Fig. A1. The two focal points are F and F', and they can be defined in the following way. Let P be an arbitrary point on the ellipse. If F is a focal point, then the two distances  $|QP|$  and  $|PF|$  are related by

$$E_c|QP| = |PF|, \tag{A1}$$

where  $E_c$  is the true eccentricity,

$$E_c = \frac{\sqrt{|AC|^2 - |CB|^2}}{|AC|} = \frac{\sqrt{|CA'|^2 - |CB'|^2}}{|CA'|} = \dots, \tag{A2}$$

and  $|AC|$ ,  $|CB|$ , etc., are the indicated distances in Fig. A1. If F is truly a focal point, Eqn. A1 holds for any and all choices of P. Next, the distance  $|OA|$  is equal to the distance  $|BC|$ , so that the vertical line Z' is the same distance from F' as F is to O. The F' is the other focal point if for all points P' on the ellipse

$$E_c|P'Q'| = |F'P'| \tag{A3}$$

The focal distance,  $c$ , is then the distance between points F and F', i.e.

$$c = |FF'| \tag{A4}$$

**APPENDIX B**

The term X in Eqns. 18 and 23 is defined by Gardiner et al. (in press) as

$$X = -\frac{Sc^2}{6D} \sinh(2\alpha_0) + C_{02} \left. \frac{dQ_0(i \sinh(\alpha))}{d\alpha} \right|_{\alpha=\alpha_0} \tag{B1}$$

where  $i$  is the square root of  $-1$ ,

$$Q_0(i \sinh(\alpha)) = \frac{1}{2} \ln \left[ \frac{1 + i \sinh(\alpha)}{1 - i \sinh(\alpha)} \right] = i \arctan(\sinh(\alpha)), \tag{B2}$$

and

$$C_{02} = \frac{k\psi_g - \psi_\infty + \frac{Sc^2}{6D} (\cosh^2(\alpha_0) - \cosh^2(\alpha_1))}{Q_0(i \sinh(\alpha_0)) - Q_0(i \sinh(\alpha_1))}. \tag{B3}$$

Even though these three equations contain the complex number  $i$ , X in Eqn. B1 is a real number.